Characterization of drusen formation in a primary porcine tissue culture model of dry AMD

Erika M. Shaw,[1] Alexander J. Tate,[1] Ramesh Periasamy,[2] and Daniel M. Lipinski[1,2]

[1]Department of Cell Biology, Neurobiology and Anatomy, Medical College of Wisconsin, Milwaukee, WI, USA; [2]Department of Ophthalmology and Visual Sciences, Medical College of Wisconsin, Milwaukee, WI, USA

Age-related macular degeneration (AMD) affects millions of individuals worldwide and is a leading cause of blindness in the elderly. In dry AMD, lipoproteinaceous deposits called drusen accumulate between the retinal pigment epithelium (RPE) and Bruch's membrane, leading to impairment of oxygen and nutrient trafficking to the neural retina, and degeneration of the overlying photoreceptor cells. Owing to key differences in human and animal ocular anatomy and the slowly progressing nature of the disease, AMD is not easily modeled *in vivo*. In this study, we further characterize a "drusen-in-a-dish" primary porcine RPE model system by employing vital lipid staining to monitor sub-RPE deposition over time in monolayers of cells cultured on porous transwell membranes. We demonstrate for the first time using a semi-automated image analysis pipeline that the number and size of sub-RPE deposits increases gradually but significantly over time and confirm that sub-RPE deposits grown in culture immunostain positive for multiple known components found in human drusen. As a result, we propose that drusen-in-a-dish cell culture models represent a high-throughput and cost-scalable alternative to animal models in which to study the pathobiology of drusen accumulation and may serve as useful tools for screening novel therapeutics aimed at treating dry AMD.

INTRODUCTION

Age-related macular degeneration (AMD) is estimated to affect approximately 8.7% of all individuals between the ages of 45 and 85 years and is a leading cause of blindness among the elderly worldwide.[1,2] This disease is classified into dry and wet forms, the former of which accounts for approximately 90% of all AMD cases and is commonly characterized by the abnormal accumulation of sub-retinal pigment epithelium (RPE) deposits called drusen.[3–6] When drusen develop within the macular region, they are hypothesized to contribute to AMD pathology directly by interfering with nutrient and oxygen cycling between the RPE and underlying choroid, resulting in a toxic buildup of waste products and ischemia, which culminates in RPE, photoreceptor atrophy, and progressive loss of central vision.[7–9] In approximately 10% of cases, the individual will progress from dry to wet AMD, which is characterized by vascular invasion into the retinal layers from the choroid, often through areas where the RPE barrier has been disrupted, leading to rapid vision loss from retinal hemorrhage, edema, and inflammation.[5,6] While wet AMD can be treated effectively through periodic bolus dosing of vascular endothelial growth factor (VEGF) inhibitors to prevent neovascularization, and two new therapeutics for late-stage dry AMD known as geographic atrophy, gained US Food and Drug Administration approval in 2023 (avacincaptad pegol and pegcetacoplan), early to intermediate dry AMD remains without any effective treatment at early stages beyond dietary supplementation with zinc, antioxidants and carotenoids via AREDS (Age-Related Eye Disease Studies) vitamins.[4,9–16]

Although the exact nature of drusen accumulation and their role in AMD pathobiology is still debated, the dynamics and composition of drusen extracted from human retinae have been extensively studied, with deposits known to contain approximately 40%–60% lipid, with the remaining deposit volume consisting of proteins (e.g., apolipoproteins and components of the complement cascade and basement membrane) and minerals (e.g., hydroxyapatite) that vary depending on the anatomical location (central versus peripheral) and drusen type (e.g., hard, soft, reticular-pseudo).[9,17,18] Interestingly, particularly in the context of the "oil spill" hypothesis of drusen formation, sub-RPE deposits have been observed to be very dynamic, constantly growing or shrinking throughout their life cycle, and eventually disappearing once the overlying RPE cells have atrophied and clearance of deposited material through choroidal outflow can reassert itself.[9,19–24]

Owing to their complex and varying composition, deposition over long time scales, and dynamic nature, drusen have been extremely difficult to model convincingly. While there are numerous genetic and environmental animal models of AMD that mimic individual characteristics of the disease pathology (e.g., sub-RPE deposit formation, RPE atrophy, photoreceptor cell death) no animal model accurately recapitulates all aspects of dry AMD disease pathology and progression.[4,25–31] Indeed, one notable and critical limitation to the use of

Correspondence: Daniel M. Lipinski, Department of Cell Biology, Neurobiology and Anatomy, Medical College of Wisconsin, Milwaukee, WI, USA.
E-mail: dlipinski@mcw.edu

animal models when studying AMD pathology is that with the exception of non-human primates (NHPs) and certain lizard (e.g., anoles) and bird (e.g., raptors) species, the majority of animals utilized in scientific research lack a defined (i.e., excavated, avascular, and containing almost exclusively cone photoreceptors) macula or fovea. In addition to a lack of a macula and other anatomical differences such as a lack of retinal vasculature, the largest risk factor for AMD development is advanced age, and most animal species do not have long enough lifespans to accumulate pathogenic numbers of drusen leading to RPE and photoreceptor atrophy, even in NHPs aged over several years.[32]

As a result of the limitations with animal models, the relative rarity of human donor tissue with confirmed AMD pathology, and the inability to perform experiments on such tissue beyond histology, there has been substantial interest in the development of novel cell and tissue culture model systems for use in AMD research. Specifically, cell culture models potentially offer a high-throughput, low-cost, and easy-to-manipulate system in which to model at least the initial stages of drusen formation, such as their deposition, growth, and dynamics, and screen the effectiveness of novel therapeutics aimed at manipulating drusen pathobiology. Here, we build upon several previous reports of "drusen-in-a-dish" models, wherein primary or induced pluripotent stem cell (iPSC)-derived RPE cultured as monolayers for extended periods of time on a porous support have been observed to develop sub-RPE deposits characteristic of human drusen.[33–35] Specifically, for the first time, we longitudinally characterize the development, composition, and dynamics of sub-RPE deposit formation over a period of 6 months using a combination of repetitive fluorescence microscopy and cross-sectional histology and employ a semi-automated analysis pipeline to accurately quantify sub-RPE deposit number and size over time. As such, this study provides the first metrics of longitudinal sub-RPE deposit dynamics in a primary RPE culture system and may serve as a model for screening therapeutics aimed at limiting drusen accumulation or shrinking drusen size, an important consideration where the presence of large, soft, or confluent drusen is a hallmark of AMD and is directly correlated to the progression of retinal atrophy and the risk of neovascularization.[13,19]

RESULTS

Sub-RPE deposit number increases gradually with extended culture duration

Primary porcine RPE cells were isolated on four separate occasions (12–15 wells per isolation, 51 wells total) and cultured on transwell tissue culture inserts for a period of up to 24 weeks, during which time the total number of sub-RPE deposits per well was visualized at 4, 8, 12, 16, 20, and 24 weeks using repetitive epi-fluorescence imaging following staining with Nile red, a non-toxic vital dye that is strongly fluorescent only in hydrophobic environments and does not "dissolve the lipids … it reveal[s]."[36,37] To confirm that deposits stained using the Nile red vital dye truly correspond to protein containing sub-RPE deposits, immunohistochemistry was performed at each time point to allow the pattern of lipid staining via Nile red to be compared directly to that of a major protein component of drusen, apolipoprotein E

(APOE; Figure S1). At each time point, an almost identical pattern of staining was observed following Nile red and APOE co-staining, strongly indicating that deposits identified through repetitive vital staining with Nile red are truly sub-RPE deposits that also contain major protein components observed in human drusen.

Tiled images of each entire well (Figure 2A) were captured to prevent area selection bias, and the resulting images were processed using a custom quantification program that automatically masks, binarizes, and thresholds each image (Figure 1) before quantifying the number of discrete fluorescent "blobs" above 700 μm^2 in total area (approximately 30 μm in diameter), which has been defined as the lower size limit for drusen to be clinically relevant in human patients with AMD.[38,39]

At 4 weeks post-isolation, the number of Nile-red positive sub-RPE deposits was low (mean = 38.71 ± 22.54 deposits per well) and showed little variability, with 82% of all wells falling within 1 SD (16.17–61.25 deposits per well) across all preparations (Figure 2B). Linear regression analysis (Figure S2) reveals an upward trend (slope = 0.7049) in sub-RPE deposit number over time that is significant ($p = 0.001111$) when the intercept is anchored on the assumption that the number of deposits at the time of cell seeding is zero (Figure S2A); however, it was not possible to empirically quantify deposit numbers at that early time point (see discussion). Groupwise comparison (one-way ANOVA with Tukey post-test) reveals a significantly greater number of sub-RPE deposits at 20 weeks (130.2 ± 144.5) compared to 4 weeks (38.71 ± 22.54; $p = 0.0021$) across all wells (Figure 2B), indicating a net accumulation of sub-RPE deposits with increasing culture age.

Interestingly, when comparing only samples that survived throughout the entire study to the 24-week endpoint, this trend is still apparent, but no longer statistically significant (Figures 2B and S2B). At the 24-week endpoint, the mean number (91.44 ± 109.2) of sub-RPE deposits was observed to be slightly but not statistically lower relative to 20 weeks (Figures 2B and 2C); however, it is unclear whether this represents a true reduction in net deposit number or is an artifact of reduced power owing to high levels of well dropout at the final time point (see discussion).

Sub-RPE deposit area increases significantly with culture duration

In addition to quantifying the net accumulation of sub-RPE deposits over time, another key aspect of our model system is the ability to accurately measure the size of sub-RPE deposits, metrics which may be critical for screening novel therapeutics aimed at reducing drusen burden in AMD by reducing lipid/protein deposition. Sub-RPE deposits were observed to be relatively but not significantly smaller at the 4-week time point (N = 51 wells; median area = 1,253 μm^2) compared to both 16-week (N = 12 wells; 1,474 μm^2) and 20-week (N = 10 wells; 1,583 μm^2) time points (Figure 3A). While these results are not significant (one-way ANOVA with Tukey post-test), linear regression reveals a positive trend in median values (R^2 = 0.5029), indicating that sub-RPE deposits increase gradually in size
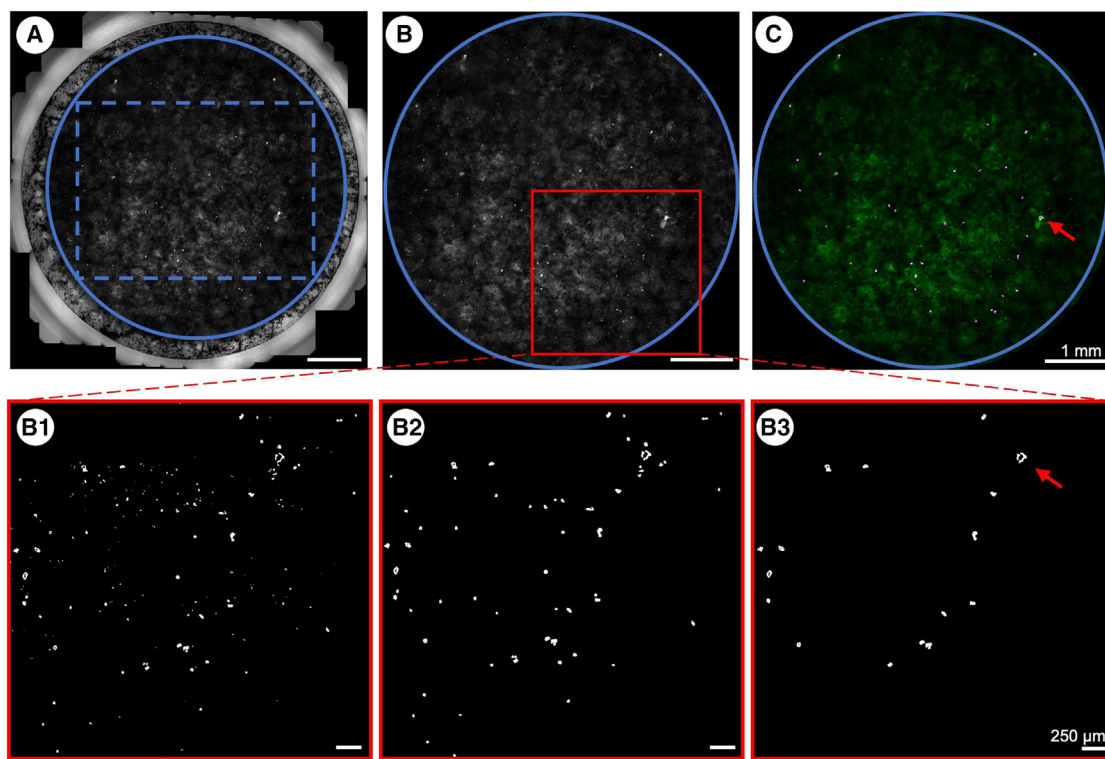
Figure 1. Sub-RPE deposit counting

A rectangle circumscribed by the interior wall of the well was defined on the raw image (A) to generate a circular mask (blue), outside of which pixel intensity was set to black (B). The image was binarized relative to background noise (B1) before initial deposit candidates were identified via blob analysis (B2). Size-adjusted deposits larger than 30 μm diameter were included for characterization (B3). Deposits were overlaid against the unprocessed, masked image to manually corroborate automated deposit detection (C). Scale bars (A–C), approximately 1 mm; (B1–B3), approximately 250 μm.

over time (Figure 3B). Interestingly, these results gain significance when comparing only samples that survived to the 24-week endpoint, where we observed a statistically significant increase in median deposit area between the 4-week time point (1,213 μm^2) and both 16-week (1,590 μm^2; $p = 0.0427$) and 20-week (1,622 μm^2; $p = 0.0141$) time points ($N = 9$) (Figures 3C and 3D).

To determine whether the observed increase in sub-RPE deposit area over time was due to a uniform increase in the size of all deposits, we plotted the size distribution of individual deposits across every well for each time point. The area distribution at all time points revealed a pronounced rightward skew toward there being a greater number of smaller deposits irrespective of culture age (Figure 3E). However, the size distribution was the most heavily right leaning at the 4-week time point, with a skewedness coefficient of 21.78 (Figure 3E). Skewness subsequently decreased to 12.46 at 8 weeks (Figure 3E), after which time, the skewness coefficient fell in the range of 3.063–3.309 for all subsequent time points (Figure 3E), indicating the formation of relatively larger deposits. When analyzed via Kolmogorov-Smirnov test, these results show statistically significant changes in distribution at the 12- ($p = 0.0003$), 16- ($p = 0.0002838$), 20- ($p = 7.317e-7$), and 24-week time points ($p = 5.539e-013$) when compared to the initial 4-week size distribution (Figure 3E). In agree-

ment with this finding, we observed via microscopy that the size of individual sub-RPE deposits was dynamic, and the majority of deposits that could be identified over multiple time points appeared to obviously increase in area (Figure S3).

Cross-sectional histology reveals presence of known drusen components is dynamic over time

In addition to performing Nile red staining at all time points—which allows for lipid containing sub-RPE deposits to be repetitively and noninvasively visualized over time for the purpose of quantifying number and size—we wanted to gain further insight into the dynamics of protein accumulation in sub-RPE deposits using cross-sectional histology and immunofluorescence staining. Compositionally, sub-RPE deposits showed positive immunofluorescence staining for numerous protein species known to be present in human drusen, including APOE, APOJ, complement factor H (CFH), complement factor I (CFI), and complement component 9 (C9) throughout many of the time points, lending credibility that such model systems recapitulate important features of drusen formation. Interestingly, we consistently observed changes in collagen V deposition over time. Specifically, areas of collagen V enrichment were sparse at the early 4- and 8-week time points, but by 12 weeks post-isolation the majority of wells examined consistently exhibited long "rafts" of collagen V located basally to the
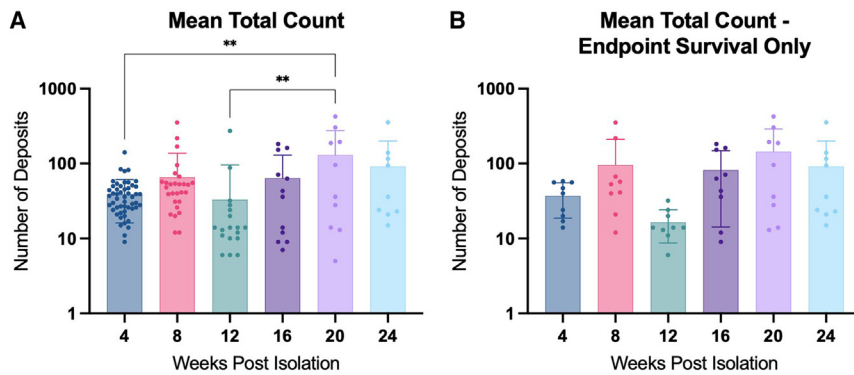
Figure 2. Total count of sub-RPE deposits over time
RPE were stained at each time point with Nile red lipid stain, and the entire well was imaged using tiling software. Deposits were quantified, and mean count with SD was reported at each time point for all wells (A). Mean total count with SD was also analyzed including only wells that survived to the 24-week endpoint (B). Data were analyzed with one-way ANOVA with Tukey's multiple comparisons. **$p < 0.01$.

RPE, which may be analogous to thickening of Bruch's membrane, a common pathogenic feature of the very earliest stages of dry AMD (Figure 4A). Conversely, CFH staining showed the greatest enrichment levels at earlier time points, but deposits decreased as the RPE aged (Figure 4B). Vitronectin staining remained relatively consistent until 24 weeks post-isolation at which point staining intensity noticeably decreased in all wells examined and across all preparations (Figure 4C). Immunofluorescence staining for other components (e.g., CFI, APOE, APOJ) did not yield any obvious or consistent alterations between time points (Figures S4 and S5). Upon bright-field imaging, RPE cell morphology remained consistent throughout the 16-week time point. At 20 weeks post-isolation, sub-RPE deposits became larger and more visually evident in cross-section (red arrow, Figure 4D). Meanwhile, at the 24-week time point, RPE morphology became abnormal as cell structures became more irregular, and increasing cellular debris indicated a decrease in overall cellular health (Figure 4D).

RPE preparations demonstrate variable survival over long culture periods

The long-term survival and integrity of the RPE monolayers is a key variable that directly affects the ability to quantify metrics (e.g., sub-RPE deposit number and size) reliably and reproducibly over time in response to experimental manipulation. To confirm that RPE cells assume and maintain a continuous monolayer with "cobblestone" morphology and express tight junction markers, which are indicative of the epithelial layer being mature and forming a continuous selectively permeable barrier, we performed immunohistochemistry for the presence of zonula occludens-1 (ZO-1) at each time point. At earlier time points (4–12 weeks), the primary porcine RPE forms a regular polygonal lattice consisting of largely mononucleated cells (Figures 5A–5C). From 16 weeks onward, RPE cell size appears to increase and the cobblestone morphology becomes increasingly irregular, with the appearance of anucleate cells by 20–24 weeks, which together suggest a decline in monolayer health over time and RPE cells expanding to maintain membrane integrity in areas of cell death (Figures 5D–5F).

Overall, RPE survival to the 12-week time point was 35.71%, with endpoint survival at 24 weeks just 23.8% (Figure 6A). Interestingly, survival was highly variable between isolations, with zero wells

from preparation 2 surviving to the 12-week time point, while 70% of RPE wells from preparation 3 survived to the same point. Endpoint survival was similarly dependent upon isolation, with survival percentages for preparations 1–4 of 25%, 0%, 30%, and 40%, respectively (Figure 6B).

Deposit count is also variable between isolations. When comparing all wells, there are no significant differences in mean deposit count or mean deposit area between isolations (Figures 6C–6E). However, when comparing only the wells that survived to the 24-week endpoint ($N = 9$), there are statistically significant differences between isolations (Figures 6D–6F). While the total number of deposits and deposit area cluster closely at the 4- and 24-week time points, when analyzed via two-way ANOVA with Tukey's multiple comparisons, there are significant differences between preparations at all other time points. This is especially evident at the 16- and 20-week time points, where preparation 4 shows statistically significant increases in mean deposit count versus preparation 1 ($p = 0.0462$) and preparation 3 ($p = 0.0364$; Figure 6D), and at the 16-week time point, the mean deposit area of preparation 3 is statistically different from that of preparation 1 ($p = 0.0430$) and preparation 4 ($p = 0.0201$; Figure 6F).

DISCUSSION

AMD is the leading cause of blindness in older adults, affecting approximately 200 million individuals worldwide and an estimated 8.7% of the population aged between 45 and 85 years.[1,2] Although the major vision-threatening symptoms of late-stage exudative disease, choroidal neovascularization and macular edema, are treatable through repetitive bolus dosing of VEGF inhibitors, dry AMD, which represents the majority (∼85%) of cases, is effectively untreatable beyond attempting to limit the risk of progression from early- to late-stage disease through dietary supplementation of zinc, antioxidants, and carotenoids.[13,14] One substantial barrier preventing the development of novel therapeutics for the treatment of dry AMD is the lack of model systems that accurately recapitulate the major pathogenic lesions of early-stage disease, namely the sub-RPE accumulation of drusen.[13,40–42] In this study, we describe a primary porcine cell culture model that provides a high-throughput and cost-scalable approach to modeling the dynamics of drusen accumulation,
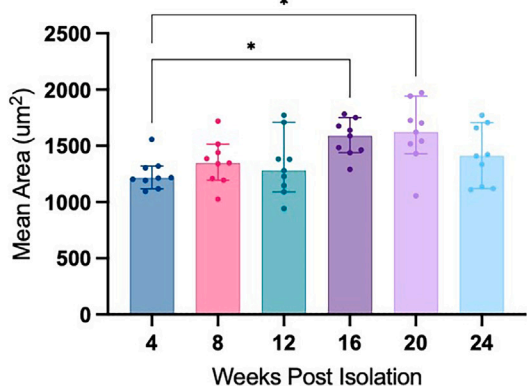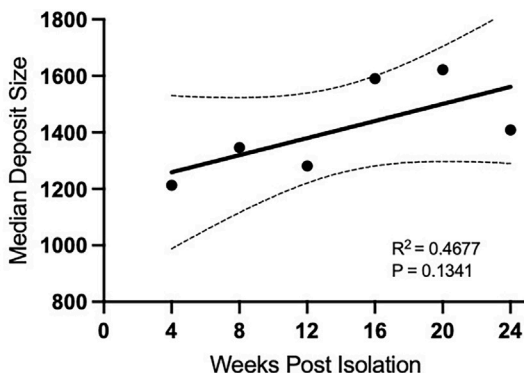
A Median Deposit Area
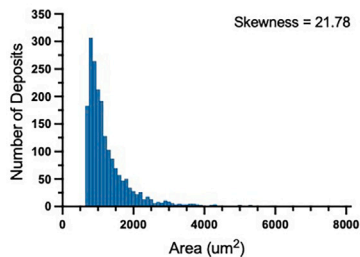
B Linear Regression of Median Deposit Size

R² = 0.5029
P = 0.1146
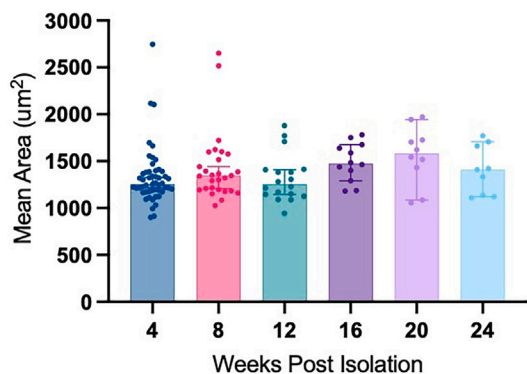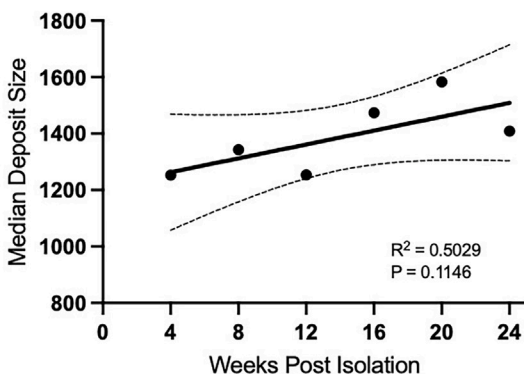
C Median Deposit Area - Endpoint Survival Only

D Linear Regression of Median Deposit Size - Endpoint Survival Only

R² = 0.4677
P = 0.1341

E

4 Week Size Distribution
Skewness = 21.78
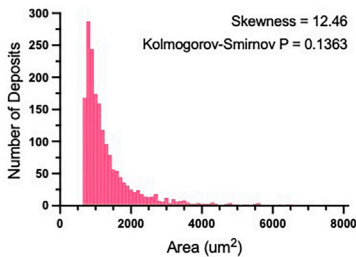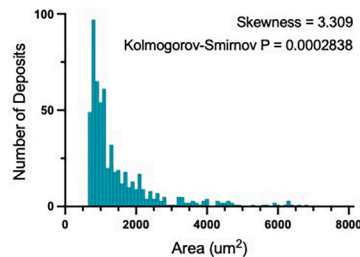
8 Week Size Distribution
Skewness = 12.46
Kolmogorov-Smirnov P = 0.1363

12 Week Size Distribution
Skewness = 3.309
Kolmogorov-Smirnov P = 0.0002838

16 Week Size Distribution
Skewness = 3.128
Kolmogorov-Smirnov P = 7.317e-007

20 Week Size Distribution
Skewness = 3.063
Kolmogorov-Smirnov P = 5.539e-013
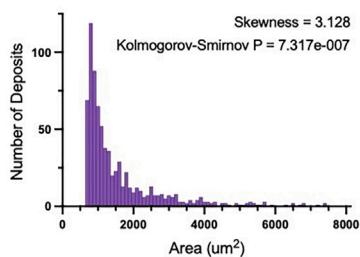
24 Week Size Distribution
Skewness = 3.068
Kolmogorov-Smirnov P = 2.908e-005
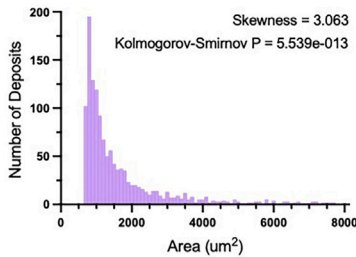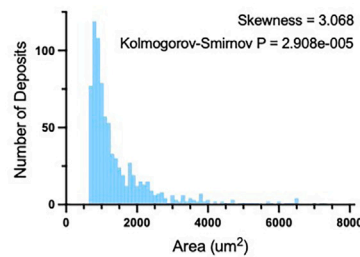
(legend on next page)

Figure 4. Histology and immunofluorescence of primary RPE

Primary RPE transwells were fixed and cryosectioned at each time point. Sections were probed for collagen V (A), CFH (B), and vitronectin (C) and visualized using confocal microscopy. Bright-field images were acquired using light microscopy, with red arrow denoting visible deposit formation (D). Scale bars, approximately 10 μm.

demonstrates that sub-RPE deposits grown in culture increase in both number and size over time, and exhibits compositional similarities to human drusen found in AMD.

Several previous studies have demonstrated that primary or iPSC-derived RPE cells grown as a monolayer on a porous support (e.g., transwell membrane) over an extended culture period (i.e., weeks or months) spontaneously develop sub-RPE lipoproteinaceous deposits that are compositionally and structurally similar to human drusen.[33–35,43,44] While it is encouraging that cultured RPE cells develop such deposits, apparently regardless of their origin (e.g., primary or iPSC derived) or host species (e.g., human, porcine, or mouse recovered) and without outer-segment supplementation, no attempt has been made to systematically characterize the dynamics of sub-RPE deposit formation. As a consequence, this has substantially limited the ability of the field to utilize these model systems to develop and

screen novel therapeutics aimed at modulating drusen pathobiology in dry AMD. In this study, we employed a custom semi-automated image analysis pipeline to quantify sub-RPE deposit number and size, allowing us to demonstrate for the first time that lab-grown drusen gradually grow in both quantity and size over time, with significant increases evident by 16 to 20 weeks compared to baseline (4 weeks). Importantly, this work provides fundamental metrics for sub-RPE deposit accumulation and a time course that could be used to set baseline expectations for the quantity and size of drusen in response to treatment—for example, following administration of peptides designed to reduced lipid load, such as APOA-I mimetics.[45,46]

That the number and size of sub-RPE deposits could be quantified using repetitive Nile red staining and fluorescence microscopy is a major strength of the model, allowing the kinetics of drusen

Figure 3. Area of sub-RPE deposits over time

Mean area of sub-RPE deposits was quantified at each time point for all wells. Median values with 95% confidence intervals were determined for all wells, and data were analyzed using one-way ANOVA with Tukey's multiple comparisons (A) and linear regression (B). Tests were also performed including only wells that survived to the 24-week endpoint (C and D). Size distributions for each deposit, including all RPE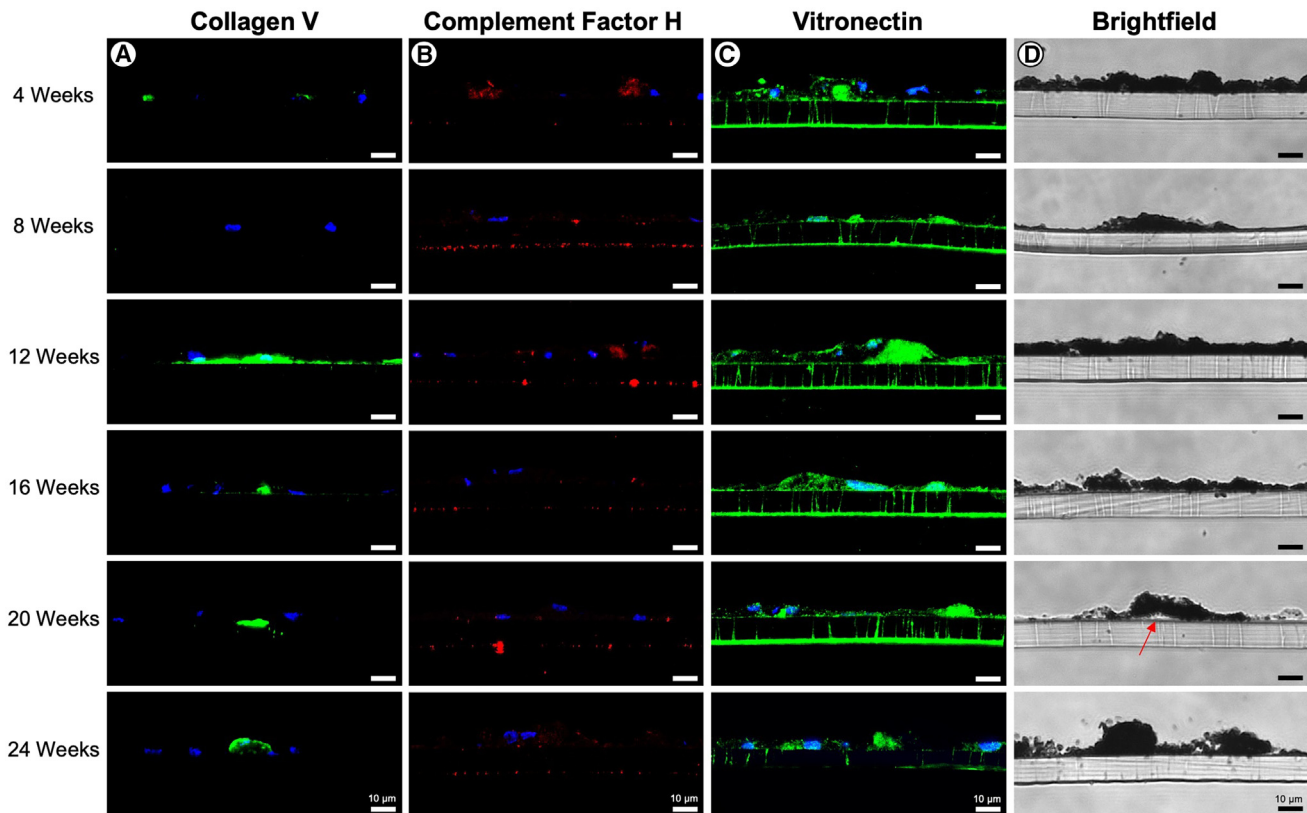 wells, were analyzed using at each time point (E, Kolmogorov-Smirnov test versus 4-week size distribution). Size distributions are restricted to values under 8,000 μm^2 for clarity (>99.3% of all values); *$p < 0.05$.

4 Weeks **8 Weeks** **12 Weeks**

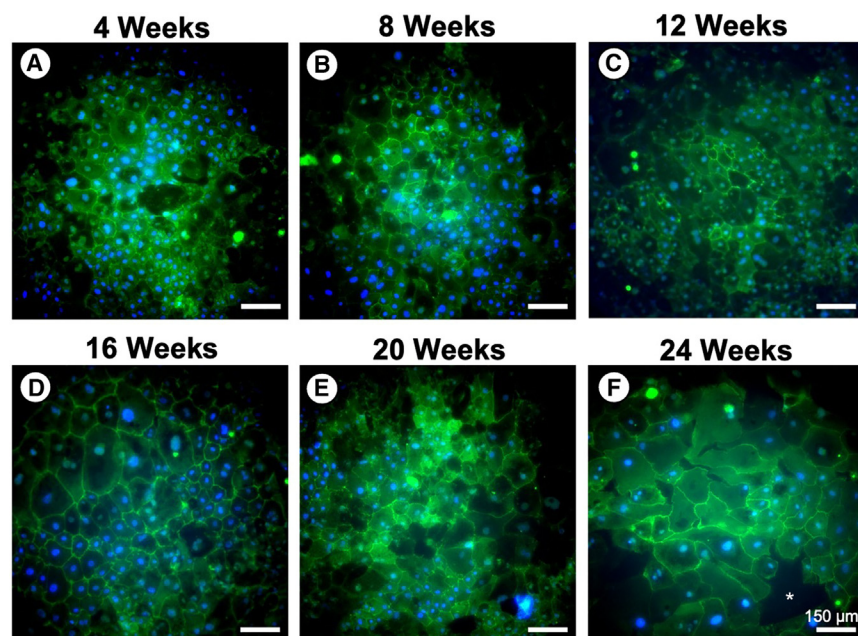**16 Weeks** **20 Weeks** **24 Weeks**

Figure 5. RPE morphology and tight junction expression

RPE monolayers harvested at each time point (A-F) were probed for ZO-1 to assess the presence of tight junctions and visualize epithelial morphology. ZO-1 staining revealed that RPE cells become increasingly dysmorphic over time, with evidence of cellular swelling, anucleated cells and areas of RPE cell death–> (*). Scale bar, 150 μm.

accumulation to be modeled longitudinally. Similar to human drusen observed in the eyes of patients with dry AMD using non-invasive *in vivo* imaging techniques, such as confocal scanning laser ophthalmoscopy, the sub-RPE deposits documented in this longitudinal study persisted throughout multiple time points and were observed to be dynamic, visibly growing, shrinking, or altering their shape over the time course (Figure S3).[9,19–24] This observation strongly implies that sub-RPE deposit accumulation in tissue culture model systems may accurately mimic the dynamic deposition and clearance of material proposed to occur in human disease, where drusen formation likely arises due to an imbalance between the aggregation of RPE-/photoreceptor-derived waste products and their clearance via the choroidal circulation.[9] While the current iteration of our image analysis code focuses only on quantifying deposit number and size globally across the well at each individual time point, because drusen are not mobile (i.e., they do not migrate laterally within the well) and transwell membranes can be consistently oriented during imaging, it may be possible to expand our pipeline to measure the size changes of individual deposits longitudinally by registering location to known landmarks, such as the well edges. Implementing this feature may be of particular importance if using this model system to study the effects of novel therapeutics aimed at reducing sub-RPE deposit size in particular, where it would be necessary to identify and track each sub-RPE deposit individually to examine the effect of therapy on growth/size.[47]

The necessity to visualize sub-RPE deposits using repetitive staining, rather than through some intrinsic property such as autofluorescence or reflectance as is possible using *in vivo* imaging of human patients with AMD, does represent a potential limitation of this model system.[48,49] Here, we utilized Nile red, which is a lipophilic dye that fluoresces strongly only in the presence of lipids and is compatible with most aqueous systems once solvated (e.g., in a polar solvent like acetonitrile), making it an ideal vital stain that can be used to detect the accumulation of lipid-rich deposits or droplets in living cells.[36] First, this means that Nile red can only be used to visualize sub-RPE deposits that contain a substantial proportion of neutral or polar lipid species, and cannot visualize deposits substantially comprising protein or mineral species, such as hydroxyapatite. As a consequence, it is likely that our approach underestimates the overall number of sub-RPE deposits as it cannot visualize accumulations containing minimal lipid that may be more reminiscent of "hard drusen." Unfortunately, to the authors' knowledge, there is no equivalent generic vital dye for staining proteins that could be used alongside Nile red to expand our staining protocol and ensure that all sub-RPE deposits are visualized regardless of composition. Second, as Nile red is internalized within the cell, the dye cannot be washed out, where loss of fluorescence occurs gradually following natural elimination of the dye from the cell. This has the effect of decreasing the resolution at which imaging can be performed—in this case to monthly assessments—as it is necessary to wait an extended period for the dye to be eliminated completely before re-staining the same cells. Third, as Nile red dye is supplied in the media, it is necessary to wash off excess dye prior to visualization to prevent overaccumulation that would increase background fluorescence levels; as such, it is likely not possible to stain at very early time points (<7–10 days) immediately following RPE isolation, where washing would disrupt cell attachment to the porous support. This inability to easily visualize sub-RPE deposit formation at very early time points may be problematic; we noted a relatively large number of smaller deposits already present at 4 weeks, indicating that drusen accumulation occurs relatively rapidly following cell seeding (Figure 2). While we did not attempt time points earlier than 4 weeks in the present study, we believe that if sufficient care were taken, then it may be possible to stain for sub-RPE deposits as early as 10 days post-isolation without adversely affecting monolayer integrity, thereby providing an earlier insight into sub-RPE deposit accumulation in this system. If staining with Nile red at time points earlier than 4 weeks cannot be performed without mechanical disruption of the RPE monolayer, however, then the utility of this model system may unfortunately be limited to the evaluation of therapeutics aiming at reducing the number or size of preexisting drusen, rather than those aimed at preventing deposition.
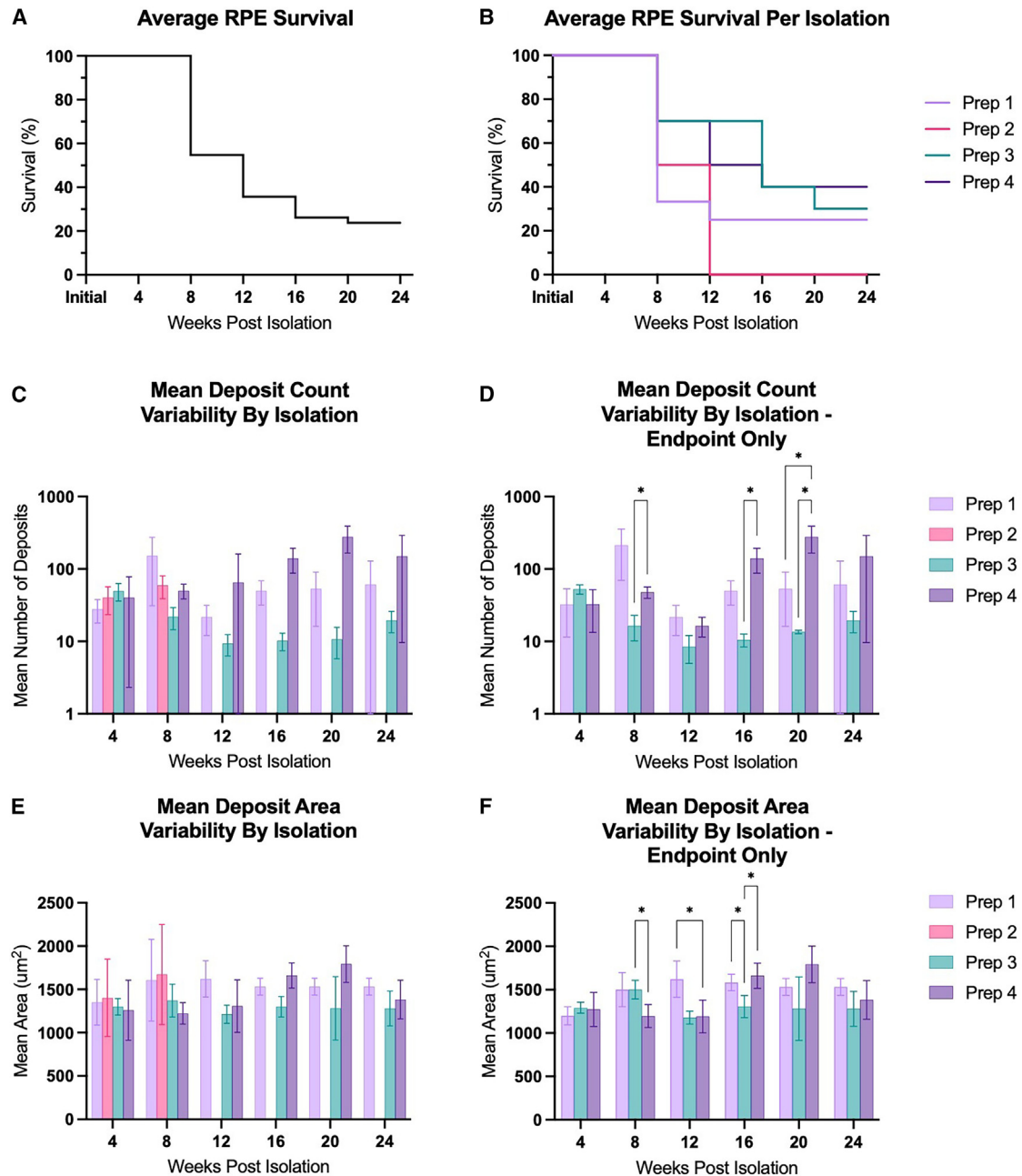
Figure 6. Survival and variability in deposit quantity and size between RPE preparations

RPE whole-well survival at each time point was determined and plotted with RPE preparations combined (A) and separated (B). Mean number of deposits with SD at each time point was graphed based on individual preparations, including all wells (C) and only those surviving to the 24-week endpoint (D). Mean deposit area with SDs for each preparation were determined for all wells and graphed including all wells (E) and endpoint surviving wells only (F). Count and area data were analyzed using two-way ANOVA with Tukey's multiple comparisons. $*p < 0.05$.

To our knowledge, this study is the first to empirically examine the survival of primary RPE monolayer cultures over time and the variability of deposit formation between RPE isolations, both critical variables affecting model usability. RPE survival across all preparations was observed to be high at early time points—100% up to 8 weeks—but dropped precipitously throughout the experimental time course, reaching 23.8% mean survival at 24 weeks (Figure 6). This suggests that studies requiring long-term follow-up would benefit from being appropriately powered to account for >75% well loss over 6 months of culture. While the low survival rate over time

was largely a result of periodic infections that necessitated wells be disposed of, despite all cell cultures being performed in a sterile manner in a biosafety cabinet and with the addition of antibiotics and antimycotics to the culture medium, staining for the tight junction marker ZO-1 also demonstrated a progressive reduction in the health and integrity of the RPE monolayer over the experimental time course (Figure 5). The observation that decreasing cellular health and monolayer integrity occurs in parallel with an increase in the number and size of sub-RPE deposits may be particularly relevant for the use of such culture systems as models of AMD. Specifically, if decreased RPE cell health and survival are related to the accumulation of large sub-RPE deposits, then this would closely model the oil spill hypothesis of AMD pathogenesis, wherein drusen are proposed to be directly pathogenic and their accumulation causes death of the overlying RPE by inhibiting oxygen and nutrient exchange and the elimination of cytotoxic waste products between the cells and the choroid.[9,50,51] As such, experimentally validating whether the accumulation of sub-RPE deposits directly affects the health of the RPE monolayer would be a critical next step in the development of this and other drusen-in-a-dish model systems. This could be achieved either through manipulation of the culture system to decrease or increase the number of drusen present, such as by supplementing the culture media with lipids or other drusen components to accelerate their growth, or by comparing RPE harvested and plated directly as in our system with primary RPE that have been passaged, which prevents the accumulation of drusen through a mechanism that is incompletely understood.[33]

When assessing only those wells that survived to 24 weeks, there is a statistically significant variability in deposit number and size by preparation, particularly at intermediate time points (i.e., 12 to 20 weeks), indicating that the dynamics of drusen accumulation may in some way be dependent upon the health of the donor tissue or success of the isolation, although we tried to control for both these variables by sourcing fresh tissue and having tissues be processed immediately by the same investigator for each preparation. Despite these efforts at standardizing tissue collection and processing, the authors acknowledge that several other variables exist, such as time from euthanasia to enucleation or age of the slaughtered animals, which are not easily controllable without using laboratory-sourced animals (i.e., swine born and housed in a vivarium for the purpose of being tissue donors) and may affect batch-to-batch survival and cellular health. In any case, it suggests that when using any RPE primary culture model, the effects of any intervention should be screened across multiple independent isolations and averaged to account for inter-preparation variability.

The authors hope that the custom semi-automated code developed as part of this study, which has been made available as shareware via GitHub, may facilitate more widespread adoption of drusen-in-a-dish model systems by dramatically decreasing the time required to perform quantification of sub-RPE deposits. Although we did not empirically measure the amount of time taken to perform manual quantification of drusen number during calibration (Figure S7), the semi-automated pipeline runs in <3 min with minimal human input and is likely at least one order of magnitude quicker. Importantly, the inclusion/exclusion criteria that determines which signals on our binarized maps are classified as a sub-RPE deposit are based upon a pre-defined size constant. As such, quantification is completely objective, in stark contrast to manual methods, where the decision to include or exclude a signal is highly subjective and would likely vary significantly between multiple human graders assessing the same image set. Indeed, the ability to objectively filter drusen by size, and to use that output to also generate longitudinal measurements of sub-RPE deposit area over time, is a major strength of our semi-automated pipeline, which would not have been possible using a manual approach. Although the size constant can be set at any value to prioritize inclusion of smaller or larger signals, in this study it was defined as being 1,590 square pixels. Accounting for the magnification factor of our imaging objective, this corresponds to a deposit with a diameter of ∼30 μm, which is defined as being the smallest size for a clinically relevant drusen in humans.[38,39] Interestingly, setting drusen size at the 1,590 square pixels threshold did lead to the automated pipeline apparently undercounting deposit numbers compared to manual counts conducted on the same subset of images (N = 10; Figure S7), although it is unclear without performing multiple manual comparisons against masked graders whether this is a systematic error inherent to the pipeline code that may require compensation. Regardless of whether there is an inherent bias toward underidentification, however, the benefits of employing a semi-automated quantification approach in terms of increased image processing speed, subject objectivity, and the type of data generated (e.g., number and area) substantially outweighs any concerns when compared to the manifest issues with performing such an analysis manually.

In summary, we present a detailed characterization of longitudinal sub-RPE deposition in a primary porcine tissue culture system that may be used to model early drusen biogenesis and pathobiology. Despite several limitations highlighted above, importantly, such model systems may be used to screen the effects of novel therapeutics aimed at modulating drusen number and size, potentially leading to the development of alternative treatments for dry AMD.

MATERIALS AND METHODS
Primary porcine RPE isolation and culture
Primary porcine RPE isolation and culture were carried out according to our previously published protocol.[43] Briefly, fresh porcine eyes were obtained from a local abattoir less than 6 h postmortem and were kept on wet ice (∼4°C) during transportation (<1 h). After the eyes were thoroughly disinfected by immersion in povidone iodine preparation solution, the cornea, lens, vitreous body, and retina were removed mechanically to expose the RPE. The primary RPE was isolated via enzymatic dissociation using two 30-min incubations in 0.25% trypsin in L-15 media at 37°C. After recovery, cells were incubated in 1% DNase I for 2 min and purified via centrifugation on a 40% Percoll cushion with 0.01 M Na_2PO_4 and 0.15 M NaCl (pH 7.4). Isolated RPE cells were plated directly on the upper

Table 1. Sample numbers of Nile red stained RPE by preparation

Preparation	4 weeks	8 weeks	12 weeks	16 weeks	20 weeks	24 weeks
1	15	6	3	3	3	3
2	12	5	–	–	–	–
3	12	8	8	5	3	2
4	12	9	7	4	4	4
Total	51	28	18	12	10	9

chambers of 24-well polyethylene terephthalate transwell membranes at a concentration of 25,000 cells per well (100,000 cells per milliliter media) in DMEM, high glucose, and HEPES cell culture medium, with 10% fetal bovine serum and 1% antibiotic-antimycotic. Primary RPEs were maintained in a 5% CO_2 and 37°C incubator, with partial media changed performed every 3–5 days for up to 24 weeks without passaging. Preparations were performed by the same researcher each time, and tissue was retrieved from the same supplier.

Nile red lipid staining, quantification, and analysis

The presence of lipid-containing sub-RPE deposits was assessed at 4, 8, 12, 16, 20, and 24 weeks post-isolation via staining with Nile red (1 μg/mL; Thermo Fisher) dissolved in 100% acetone. Nile red was diluted 1:1,000 in PBS and filtered using a 30-μm filter to remove any large particulates prior to staining. RPE cultures were first washed once with pre-warmed PBS and incubated in Nile red-PBS solution for 15 min at room temperature. Nile red-PBS was subsequently removed, and the cells were washed three times with PBS, during which time the cells were protected from light exposure. Stained deposits were visualized using an epi-fluorescence microscope (Leica DMIL), and the entire contents of each transwell membrane was imaged using live tiling software (Image Pro Insight, Media Cybernetics). The numbers of surviving wells are listed in Table 1.

Semi-automated quantification of sub-RPE deposit number and size

Tiled images encompassing the entire well area were uploaded to MATLAB for image processing and deposit quantification. A rectangular region extending from any four points at the well edge was placed manually from which an inverse circular mask circumscribing the rectangular region was generated for the purpose of excluding tiling and reflective artifacts at the periphery of the images (Figure 1A). Masked images were stored as 8-bit grayscale images for image processing. The local SD at each pixel in a 7.3 × 7.3-μm (11 pixel × 11 pixel) neighborhood was used to filter the image for relative changes in local variance and was binarized according to whether the local variance exceeded background variance (Figure 1B1). Following binarization, the native MATLAB cell-counting algorithm (*blob.analysis*) was employed to identify all deposit candidates above a minimum size of 15 μm in diameter (Figure 1B2). In addition to quantifying deposit number, the area was calculated using a bounding box analysis that assumed that deposits were ellipsoid and solid.

Based on the magnification factor of our microscope (Leica DMIL, 10× objective), in our images a 30-μm diameter circle corresponds to an area of 1,590 square pixels; as such, deposits with bounding boxes where the area of the largest inscribed ellipse was less than 1,590 square pixels were excluded from analysis (Figure 1B3). Before final deposit quantification, a simple user interface utilizing deposit indices was output from the cell-counting algorithm to allow for the manual exclusion of blobs from analysis, if necessary, such as where deposits were obscured by apparent debris, overlapping, or overestimated in regions of high cellular autofluorescence. Once size and manual exclusions were complete, the indexed deposits were updated, and characterizations of the deposits were stored and summarized for export. Images at each stage of processing were saved automatically, including an overlay of the final selected deposits and the raw, masked image for visual corroboration of the data (Figure 1C). The source code and example data for this pipeline are available as open source at https://github.com/daniellipinski/RPE_blob_analysis_pipeline.

Immunofluorescence

At each time point, one well from each RPE preparation ($N = 4$; weeks 4, 8, and 12 from preparations 1–4); $N = 3$; weeks 16, 20, and 24 weeks from preparations 1, 3, and 4) were fixed for histological analysis. Cells were washed once with PBS and fixed in 4% paraformaldehyde in PBS for 30 min at room temperature. Transwell membranes were cryoprotected using sucrose series, cryosectioned, and stained according to previously published protocols.[43] Slides were permeabilized for 20 min in 1% Triton X-100 in PBS, blocked for 1 h at room temperature (25°C) in 10% normal donkey serum in 0.05% PBS-Tween (PBST), and incubated with primary antibody overnight at 4°C in 2.5% normal donkey serum in PBST, with three washes in PBST between steps. After removal of primary antibody and three washes in PBST, slides were incubated for 1 h at 25°C in an appropriate secondary antibody (AlexaFluor, Thermo Fisher Scientific) at 1:1,000 dilution in 0.1% Triton X-100, washed in PBST, and then counterstained with Hoechst 33342 and mounted. Antibodies and dilutions can be found in Table 2.

Statistics

Sub-RPE deposit quantities and areas were analyzed using one-way ANOVA with Tukey multiple comparisons test (95% confidence level, $\alpha = 0.05$) to compare quantities between time points. Size distributions were analyzed using the Kolmogorov-Smirnov test. Variability between preparations was analyzed using two-way ANOVA with the Tukey multiple comparisons test. All statistical analyses, linear regressions, frequency distributions, and graphs were generated using GraphPad Prism 10.

DATA AND CODE AVAILABILITY

Source code and example data are openly available at https://github.com/daniellipinski/RPE_blob_analysis_pipeline. All other data will be made available upon reasonable request to the corresponding author.

Table 2. Antibodies and concentrations

Reagent	Figure	Concentration	Supplier	Identifier
Collagen type V polyclonal antibody	4A	1:200	Thermo Fisher Scientific	Rockland 600-401107-01
Complement factor H monoclonal antibody	4B	1:100	Thermo Fisher Scientific	Invitrogen GAU 018-03-03
Vitronectin polyclonal antibody	4C	1:100	Thermo Fisher Scientific	Proteintech 15833-1-AP
Complement factor I polyclonal antibody	S4A	1:100	Thermo Fisher Scientific	Invitrogen PA5-96371
Complement C9 polyclonal antibody	S4B	1:100	Thermo Fisher Scientific	Invitrogen PA5-29093
Laminin monoclonal antibody	S4C	1:100	Thermo Fisher Scientific	Invitrogen MA1-06100
APOE polylclonal antibody	S5A	1:100	Thermo Fisher Scientific	Invitrogen PA5-18361
APOJ polyclonal antibody	S5B	1:100	Thermo Fisher Scientific	Invitrogen PA5-46931

AUTHOR CONTRIBUTIONS

E.M.S. and D.M.L. designed and planned the experiments. E.M.S. performed experiments and collected and analyzed data. A.J.T. designed and modified the MATLAB code. E.M.S. and A.J.T. prepared the figures. All authors wrote and edited the manuscript.

DECLARATION OF INTERESTS

The authors declare no competing interests.

SUPPLEMENTAL INFORMATION

Supplemental information can be found online at https://doi.org/10.1016/j.omtm.2024.101331.

REFERENCES

1. Rein, D.B., Wittenborn, J.S., Burke-Conte, Z., Gulia, R., Robalik, T., Ehrlich, J.R., Lundeen, E.A., and Flaxman, A.D. (2022). Prevalence of Age-Related Macular Degeneration in the US in 2019. JAMA Ophthalmol. 140, 1202–1208. https://doi.org/10.1001/jamaophthalmol.2022.4401.

2. Wong, W.L., Su, X., Li, X., Cheung, C.M.G., Klein, R., Cheng, C.Y., and Wong, T.Y. (2014). Global prevalence of age-related macular degeneration and disease burden projection for 2020 and 2040: A systematic review and meta-analysis. Lancet. Glob. Health 2, e106–e116. https://doi.org/10.1016/S2214-109X(13)70145-1.

3. Chew, E.Y., Clemons, T.E., Agrón, E., Sperduto, R.D., SanGiovanni, J.P., Davis, M.D., and Ferris, F.L.; Age-Related Eye Disease Study Research Group (2014). Ten-year follow-up of age-related macular degeneration in the age-related eye disease study: AREDS report No. 36. JAMA Ophthalmol. 132, 272–277. https://doi.org/10.1001/jamaophthalmol.2013.6636.

4. Handa, J.T., Bowes Rickman, C., Dick, A.D., Gorin, M.B., Miller, J.W., Toth, C.A., Ueffing, M., Zarbin, M., and Farrer, L.A. (2019). A systems biology approach towards understanding and treating non-neovascular age-related macular degeneration. Nat. Commun. 10, 3347. https://doi.org/10.1038/s41467-019-11262-1.

5. Deng, Y., Qiao, L., Du, M., Qu, C., Wan, L., Li, J., and Huang, L. (2022). Age-related macular degeneration: Epidemiology, genetics, pathophysiology, diagnosis, and targeted therapy. Genes Dis. 9, 62–79. https://doi.org/10.1016/j.gendis.2021.02.009.

6. Lim, L.S., Mitchell, P., Seddon, J.M., Holz, F.G., and Wong, T.Y. (2012). Age-related macular degeneration. Lancet 379, 1728–1738. https://doi.org/10.1016/S0140-6736(12)60282-7.

7. Cankova, Z., Huang, J.D., Kruth, H.S., and Johnson, M. (2011). Passage of low-density lipoproteins through Bruch's membrane and choroid. Exp. Eye Res. 93, 947–955. https://doi.org/10.1016/j.exer.2011.10.016.

8. Linsenmeier, R.A., and Zhang, H.F. (2017). Retinal oxygen: from animals to humans. Prog. Retin. Eye Res. 58, 115–151. https://doi.org/10.1016/j.preteyeres.2017.01.003.

9. Curcio, C.A. (2018). Soft Drusen in Age-Related Macular Degeneration: Biology and Targeting Via the Oil Spill Strategies. Invest. Ophthalmol. Vis. Sci. 59, AMD160–AMD181. https://doi.org/10.1167/iovs.18-24882.

10. Al-Zamil, W.M., and Yassin, S.A. (2017). Recent developments in age-related macular degeneration: a review. Clin. Interv. Aging 12, 1313–1330. https://doi.org/10.2147/CIA.S143508.

11. Fabre, M., Mateo, L., Lamaa, D., Baillif, S., Pagès, G., Demange, L., Ronco, C., and Benhida, R. (2022). Recent Advances in Age-Related Macular Degeneration Therapies. Molecules 27, 5089. https://doi.org/10.3390/molecules27165089.

12. Rosenfeld, P.J., Brown, D.M., Heier, J.S., Boyer, D.S., Kaiser, P.K., Chung, C.Y., and Kim, R.Y.; MARINA Study Group (2006). Ranibizumab for neovascular age-related macular degeneration. N. Engl. J. Med. 355, 1419–1431. https://doi.org/10.1056/NEJMoa054481.

13. Hadziahmetovic, M., and Malek, G. (2020). Age-Related Macular Degeneration Revisited: From Pathology and Cellular Stress to Potential Therapies. Front. Cell Dev. Biol. 8, 612812. https://doi.org/10.3389/fcell.2020.612812.

14. Age-Related Eye Disease Study Research Group (2001). A randomized, placebo-controlled, clinical trial of high-dose supplementation with vitamins C and E, beta carotene, and zinc for age-related macular degeneration and vision loss: AREDS report no. 8. Arch. Ophthalmol. 119, 1417–1436. https://doi.org/10.1001/archopht.119.10.1417.

15. Heier, J.S., Lad, E.M., Holz, F.G., Rosenfeld, P.J., Guymer, R.H., Boyer, D., Grossi, F., Baumal, C.R., Korobelnik, J.F., Slakter, J.S., et al. (2023). Pegcetacoplan for the treatment of geographic atrophy secondary to age-related macular degeneration (OAKS and DERBY): two multicentre, randomised, double-masked, sham-controlled, phase 3 trials. Lancet 402, 1434–1448. https://doi.org/10.1016/S0140-6736(23)01520-9.

16. Khanani, A.M., Patel, S.S., Staurenghi, G., Tadayoni, R., Danzig, C.J., Eichenbaum, D.A., Hsu, J., Wykoff, C.C., Heier, J.S., Lally, D.R., et al. (2023). Efficacy and safety of avacincaptad pegol in patients with geographic atrophy (GATHER2): 12-month results from a randomised, double-masked, phase 3 trial. Lancet 402, 1449–1458. https://doi.org/10.1016/S0140-6736(23)01583-0.

17. Wang, L., Clark, M.E., Crossman, D.K., Kojima, K., Messinger, J.D., Mobley, J.A., and Curcio, C.A. (2010). Abundant lipid and protein components of drusen. PLoS One 5, e10329. https://doi.org/10.1371/journal.pone.0010329.

18. Crabb, J.W., Miyagi, M., Gu, X., Shadrach, K., West, K.A., Sakaguchi, H., Kamei, M., Hasan, A., Yan, L., Rayborn, M.E., et al. (2002). Drusen proteome analysis: an approach to the etiology of age-related macular degeneration. Proc. Natl. Acad. Sci. USA 99, 14682–14687. https://doi.org/10.1073/pnas.222551899.

19. Schlanitz, F.G., Baumann, B., Kundi, M., Sacu, S., Baratsits, M., Scheschy, U., Shahlaee, A., Mittermüller, T.J., Montuoro, A., Roberts, P., et al. (2017). Drusen volume development over time and its relevance to the course of age-related macular degeneration. Br. J. Ophthalmol. 101, 198–203. https://doi.org/10.1136/bjophthalmol-2016-308422.

20. Yehoshua, Z., Wang, F., Rosenfeld, P.J., Penha, F.M., Feuer, W.J., and Gregori, G. (2011). Natural history of drusen morphology in age-related macular degeneration using spectral domain optical coherence tomography. Ophthalmology 118, 2434–2441. https://doi.org/10.1016/j.ophtha.2011.05.008.

21. Sebag, M., Peli, E., and Lahav, M. (1991). Image analysis of changes in drusen area. Acta Ophthalmol. 69, 603–610. https://doi.org/10.1111/j.1755-3768.1991.tb04847.x.

22. Bressler, N.M., Munoz, B., Maguire, M.G., Vitale, S.E., Schein, O.D., Taylor, H.R., and West, S.K. (1995). Five-year incidence and disappearance of drusen and retinal pigment epithelial abnormalities. Waterman study. Arch. Ophthalmol. 113, 301–308. https://doi.org/10.1001/archopht.1995.01100030055022.

23. Sarks, J.P., Sarks, S.H., and Killingsworth, M.C. (1994). Evolution of soft drusen in age-related macular degeneration. Eye 8, 269–283. https://doi.org/10.1038/eye.1994.57.

24. Smith, R.T., Sohrab, M.A., Pumariega, N., Chen, Y., Chen, J., Lee, N., and Laine, A. (2010). Dynamic soft drusen remodelling in age-related macular degeneration. Br. J. Ophthalmol. 94, 1618–1623. https://doi.org/10.1136/bjo.2009.166843.

25. Toomey, C.B., Kelly, U., Saban, D.R., and Bowes Rickman, C. (2015). Regulation of age-related macular degeneration-like pathology by complement factor H. Proc. Natl. Acad. Sci. USA 112, E3040–E3049. https://doi.org/10.1073/pnas.1424391112.

26. Hollyfield, J.G., Bonilha, V.L., Rayborn, M.E., Yang, X., Shadrach, K.G., Lu, L., Ufret, R.L., Salomon, R.G., and Perez, V.L. (2008). Oxidative damage-induced inflammation initiates age-related macular degeneration. Nat. Med. 14, 194–198. https://doi.org/10.1038/nm1709.

27. Malek, G., Johnson, L.V., Mace, B.E., Saloupis, P., Schmechel, D.E., Rickman, D.W., Toth, C.A., Sullivan, P.M., and Bowes Rickman, C. (2005). Apolipoprotein E allele-dependent pathogenesis: a model for age-related retinal degeneration. Proc. Natl. Acad. Sci. USA 102, 11900–11905. https://doi.org/10.1073/pnas.0503015102.

28. Kaneko, H., Dridi, S., Tarallo, V., Gelfand, B.D., Fowler, B.J., Cho, W.G., Kleinman, M.E., Ponicsan, S.L., Hauswirth, W.W., Chiodo, V.A., et al. (2011). DICER1 deficit induces Alu RNA toxicity in age-related macular degeneration. Nature 471, 325–330. https://doi.org/10.1038/nature09830.

29. Nakayama, M., Iejima, D., Akahori, M., Kamei, J., Goto, A., and Iwata, T. (2014). Overexpression of HtrA1 and exposure to mainstream cigarette smoke leads to choroidal neovascularization and subretinal deposits in aged mice. Invest. Ophthalmol. Vis. Sci. 55, 6514–6523. https://doi.org/10.1167/iovs.14-14453.

30. Pennesi, M.E., Neuringer, M., and Courtney, R.J. (2012). Animal models of age related macular degeneration. Mol. Aspects Med. 33, 487–509. https://doi.org/10.1016/j.mam.2012.06.003.

31. Soundara Pandi, S.P., Ratnayaka, J.A., Lotery, A.J., and Teeling, J.L. (2021). Progress in developing rodent models of age-related macular degeneration (AMD). Exp. Eye Res. 203, 108404. https://doi.org/10.1016/j.exer.2020.108404.

32. Anderson, M., Dawson, W.W., Gonzalez-Martinez, J., and Curcio, C.A. (2006). Drusen and lipid-filled retinal pigment epithelium cells in a rhesus macula. Vet. Ophthalmol. 9, 201–207. https://doi.org/10.1111/j.1463-5224.2006.00463.x.

33. Pilgrim, M.G., Lengyel, I., Lanzirotti, A., Newville, M., Fearn, S., Emri, E., Knowles, J.C., Messinger, J.D., Read, R.W., Guidry, C., and Curcio, C.A. (2017). Subretinal pigment epithelial deposition of drusen components including hydroxyapatite in a primary cell culture model. Invest. Ophthalmol. Vis. Sci. 58, 708–719. https://doi.org/10.1167/iovs.16-21060.

34. Galloway, C.A., Dalvi, S., Hung, S.S.C., MacDonald, L.A., Latchney, L.R., Wong, R.C.B., Guymer, R.H., Mackey, D.A., Williams, D.S., Chung, M.M., et al. (2017). Drusen in patient-derived hiPSC-RPE models of macular dystrophies. Proc. Natl. Acad. Sci. USA 114, E8214–E8223. https://doi.org/10.1073/pnas.1710430114.

35. Lynn, S.A., Ward, G., Keeling, E., Scott, J.A., Cree, A.J., Johnston, D.A., Page, A., Cuan-Urquizo, E., Bhaskar, A., Grossel, M.C., et al. (2017). Ex-vivo models of the Retinal Pigment Epithelium (RPE) in long-term culture faithfully recapitulate key structural and physiological features of native RPE. Tissue Cell 49, 447–460. https://doi.org/10.1016/j.tice.2017.06.003.

36. Greenspan, P., Mayer, E.P., and Fowler, S.D. (1985). Nile red: a selective fluorescent stain for intracellular lipid droplets. J. Cell Biol. 100, 965–973. https://doi.org/10.1083/jcb.100.3.965.

37. Thompson, R.B., Reffatto, V., Bundy, J.G., Kortvely, E., Flinn, J.M., Lanzirotti, A., Jones, E.A., McPhail, D.S., Fearn, S., Boldt, K., et al. (2015). Identification of hydroxy-apatite spherules provides new insight into subretinal pigment epithelial deposit formation in the aging eye. Proc. Natl. Acad. Sci. USA 112, 1565–1570. https://doi.org/10.1073/pnas.1413347112.

38. Rudolf, M., Seckerdieck, K., Grisanti, S., and Curcio, C.A. (2014). Internal structure consistent with remodelling in very small drusen, revealed by filipin histochemistry for esterified cholesterol. Br. J. Ophthalmol. 98, 698–702. https://doi.org/10.1136/bjophthalmol-2013-304226.

39. Klein, R., Myers, C.E., Lee, K.E., Gangnon, R.E., Sivakumaran, T.A., Iyengar, S.K., and Klein, B.E.K. (2015). Small Drusen and Age-Related Macular Degeneration: The Beaver Dam Eye Study. J. Clin. Med. 4, 424–440. https://doi.org/10.3390/jcm4030425.

40. Wang, J.J., Rochtchina, E., Lee, A.J., Chia, E.M., Smith, W., Cumming, R.G., and Mitchell, P. (2007). Ten-year incidence and progression of age-related maculopathy: the blue Mountains Eye Study. Ophthalmology 114, 92–98. https://doi.org/10.1016/j.ophtha.2006.07.017.

41. Joachim, N., Mitchell, P., Burlutsky, G., Kifley, A., and Wang, J.J. (2015). The Incidence and Progression of Age-Related Macular Degeneration over 15 Years: The Blue Mountains Eye Study. Ophthalmology 122, 2482–2489. https://doi.org/10.1016/j.ophtha.2015.08.002.

42. Pollreisz, A., Reiter, G.S., Bogunovic, H., Baumann, L., Jakob, A., Schlanitz, F.G., Sacu, S., Owsley, C., Sloan, K.R., Curcio, C.A., and Schmidt-Erfurth, U. (2021). Topographic Distribution and Progression of Soft Drusen Volume in Age-Related Macular Degeneration Implicate Neurobiology of Fovea. Invest. Ophthalmol. Vis. Sci. 62, 26. https://doi.org/10.1167/iovs.62.2.26.

43. Hood, E.M.S., Curcio, C.A., and Lipinski, D. (2022). Isolation, culture, and cryosectioning of primary porcine retinal pigment epithelium on transwell cell culture inserts. STAR Protoc. 3, 101758. https://doi.org/10.1016/j.xpro.2022.101758.

44. Johnson, L.V., Forest, D.L., Banna, C.D., Radeke, C.M., Maloney, M.A., Hu, J., Spencer, C.N., Walker, A.M., Tsie, M.S., Bok, D., et al. (2011). Cell culture model that mimics drusen formation and triggers complement activation associated with age-related macular degeneration. Proc. Natl. Acad. Sci. USA 108, 18277–18282. https://doi.org/10.1073/pnas.1109703108.

45. Rudolf, M., Mir Mohi Sefat, A., Miura, Y., Tura, A., Raasch, W., Ranjbar, M., Grisanti, S., Aherrahrou, Z., Wagner, A., Messinger, J.D., et al. (2018). ApoA-I Mimetic Peptide 4F Reduces Age-Related Lipid Deposition in Murine Bruch's Membrane and Causes Its Structural Remodeling. Curr. Eye Res. 43, 135–146. https://doi.org/10.1080/02713683.2017.1370118.

46. Rudolf, M., Curcio, C.A., Schlötzer-Schrehardt, U., Sefat, A.M.M., Tura, A., Aherrahrou, Z., Brinkmann, M., Grisanti, S., Miura, Y., and Ranjbar, M. (2019). Apolipoprotein A-I Mimetic Peptide L-4F Removes Bruch's Membrane Lipids in Aged Nonhuman Primates. Invest. Ophthalmol. Vis. Sci. 60, 461–472. https://doi.org/10.1167/iovs.18-25786.

47. Guymer, R.H., Wu, Z., Hodgson, L.A.B., Caruso, E., Brassington, K.H., Tindill, N., Aung, K.Z., McGuinness, M.B., Fletcher, E.L., Chen, F.K., et al. (2019). Subthreshold Nanosecond Laser Intervention in Age-Related Macular Degeneration: The LEAD Randomized Controlled Clinical Trial. Ophthalmology 126, 829–838. https://doi.org/10.1016/j.ophtha.2018.09.015.

48. Hammer, M., Schultz, R., Hasan, S., Sauer, L., Klemm, M., Kreilkamp, L., Zweifel, L., Augsten, R., and Meller, D. (2020). Fundus Autofluorescence Lifetimes and Spectral Features of Soft Drusen and Hyperpigmentation in Age-Related Macular Degeneration. Transl. Vis. Sci. Technol. 9, 20. https://doi.org/10.1167/tvst.9.5.20.

49. Zhang, X., and Sivaprasad, S. (2021). Drusen and pachydrusen: the definition, pathogenesis, and clinical significance. Eye 35, 121–133. https://doi.org/10.1038/s41433-020-01265-4.

50. Curcio, C.A., Johnson, M., Rudolf, M., and Huang, J.D. (2011). The oil spill in ageing Bruch membrane. Br. J. Ophthalmol. 95, 1638–1645. https://doi.org/10.1136/bjophthalmol-2011-300344.

51. Tong, Y., Ach, T., Curcio, C.A., and Smith, R.T. (2021). Hyperspectral autofluorescence characterization of drusen and sub-RPE deposits in age-related macular degeneration. Ann. Eye Sci. 6, 4. https://doi.org/10.21037/aes-20-12.